ADVANCED MATERIALS
www.advmat.de

A 3D-Printed Ferromagnetic Liquid Crystal Elastomer with Programmed Dual-Anisotropy and Multi-Responsiveness

Yuxuan Sun, Liu Wang, Zhengqing Zhu, Xingxiang Li, Hong Sun, Yong Zhao, Chenhui Peng, Ji Liu,* Shiwu Zhang,* and Mujun Li**

Liquid crystal elastomers (LCE) and magnetic soft materials are promising active materials in many emerging fields, such as soft robotics. Despite the high demand for developing active materials that combine the advantages of LCE and magnetic actuation, the lack of independent programming of the LCE nematic order and magnetization in a single material still hinders the desired multi-responsiveness. In this study, a ferromagnetic LCE (magLCE) ink with nematic order and magnetization is developed that can be independently programmed to be anisotropic, referred to as "dual anisotropy", via a customized 3D-printing platform. The magLCE ink is fabricated by dispersing ferromagnetic microparticles in the LCE matrix, and a 3D-printing platform is created by integrating a magnet with 3-DoF motion into an extrusion-based 3D printer. In addition to magnetic fields, magLCEs can also be actuated by heating sources (either environmental heating or photo-heating of the embedded ferromagnetic microparticles) with a high energy density and tunable actuation temperature. A programmed magLCE strip robot is demonstrated with enhanced adaptability to complex environments (different terrains, magnetic fields, and temperatures) using a multi-actuation strategy. The magLCE also has potential applications in mechanical memory, as demonstrated by the multistable mechanical metastructure array with remote writability and stable memory.

1. Introduction

Active materials capable of stimuli-responsive deformations have significant potential in various fields, including soft robotics,[1] intelligent devices,[2] and biomedicine.[3] Among these, liquid crystal elastomers (LCEs) have attracted significant attention because of their large reversible deformations and high energy densities.[4] When activated, the aligned mesogens in the LCEs are reoriented, leading to a large contraction along the direction of the nematic order **n**. The commonly used strategies for activating LCEs include environmental heating (e.g., using an oven and heat gun), photo-thermal effects (e.g., LCEs with light-absorbing carbon nano-tubes,[5] Au nano-rod,[6] and liquid metals[7]), and chemical reactions (e.g., *cis–trans* conformational changes with azobenzene dye[8]). For example, He et al. presented a thermally actuated tubular LCE actuator for soft grippers and untethered soft robotics applications.[9] Wang et al.

Y. Sun, Z. Zhu, X. Li, H. Sun, Y. Zhao, S. Zhang, M. Li
Department of Precision Machinery and Precision Instrumentation
University of Science and Technology of China
Hefei 230026, P. R. China
E-mail: swzhang@ustc.edu.cn; lmn@ustc.edu.cn

L. Wang
CAS Key Laboratory of Mechanical Behavior and Design of Materials
Department of Modern Mechanics
University of Science and Technology of China
Hefei, Anhui 230026, P. R. China
E-mail: wangliu05@ustc.edu.cn

L. Wang
State Key Laboratory of Nonlinear Mechanics
Institute of Mechanics
Chinese Academy of Science
15 Beisihuan West Road, Beijing 100190, P. R. China

C. Peng
Department of Physics
University of Science and Technology of China
Hefei, Anhui 230026, P. R. China

J. Liu
Department of Mechanical and Energy Engineering
Southern University of Science and Technology of China
Shenzhen 518055, P. R. China
E-mail: liuj9@sustech.edu.cn

J. Liu
Shenzhen Key Laboratory of Biomimetic Robotics and Intelligent Systems
Department of Mechanical and Energy Engineering
Southern University of Science and Technology
Shenzhen 518055, P. R. China

J. Liu
Shenzhen Key Laboratory of Intelligent Robotics and Flexible Manufacturing Systems
Southern University of Science and Technology
Shenzhen 518055, P. R. China

J. Liu
Guangdong Provincial Key Laboratory of Human-Augmentation and Rehabilitation Robotics in Universities
Southern University of Science and Technology
Shenzhen 518055, P. R. China

The ORCID identification number(s) for the author(s) of this article can be found under https://doi.org/10.1002/adma.202302824

DOI: 10.1002/adma.202302824

mixed Au nanorod into an LCE matrix and used near-infrared light to achieve repeated photoresponsive actuation.[6b]

Another promising active material is magnetic soft materials, which are created by doping magnetic particles in soft polymer matrices, followed by programming the magnetization **m**.[10] When subjected to a magnetic field, magnetic soft materials generally quickly deform with a response time of ≈0.1 s.[11] Because of the high biocompatibility and penetration capability of magnetic fields, magnetic soft materials have been widely demonstrated to have promising applications in biomedicine.[12] For example, Yang et al. designed an implantable magnetic bladder that can assist patients with underactive bladders in urinating by remotely applying magnetic fields.[13] Hu et al. designed a magnetic strip robot that can perform drug delivery by adapting to different environments in the human body under magnetic control.[14]

Recently, active materials that possess the advantages of both LCE and magnetic soft materials (hereafter referred to as magnetic LCE) have been proposed to achieve multi-responsiveness, enhanced environmental adaptability, and multitasking capability. A representative work is from Zhang et al. who reported magLCE films by distributing NdFeB in an RM257-ST3866 LCE, and realized independent magnetic and thermal actuation modes.[15] Li et al. developed a magLCE bug robot with 3D mesostructures and demonstrated its adaptability to magnetic fields and heating environment.[16] However, because magnetic LCEs are still in their infancy, existing magnetic LCEs are only fabricated by a molding-based method with limited programmability (e.g., magnetizing the entire magnetic LCE with an impulse magnetic field after curing[15]), whereas independent programming of the nematic order **n** and magnetization **m** in a local domain of the magLCE has not been realized (see Table S1, Supporting Information).

In contrast to molding-based approaches, 3D printing has recently emerged as a prominent technique for customizing and programming the responsiveness of active materials.[17] For example, Kotikian et al. spatially programmed the nematic order direction of LCE by utilizing the shear-induced alignment of mesogens during 3D printing.[18] Wang et al. programmed the nematic order strength by changing the height and temperature of the printhead.[19] Kim et al. integrated an electromagnet into a printer nozzle, enabling programmable magnetization in magnetic soft materials.[11] Xu et al. realized 3D magnetization of magnetic soft materials by integrating a 2-DoF magnet into a DLP printer.[20] However, to date, 3D printing has mainly been demonstrated for programming a single functional domain (e.g., LCE mesogen or magnetic domain) in active materials. To the best of our knowledge, no study has been conducted on 3D printing that shows simultaneous programming of multiple functional domains, including the recently emerged magnetic LCEs.[21]

Herein, we propose a ferromagnetic LCE (magLCE) ink with nematic order **n** and magnetization **m** that can be independently programmed using a customized 3D-printing system (**Figure 1**a). The magLCE ink was fabricated by dispersing ferromagnetic microparticles (i.e., NdFeB with an average diameter of ≈5 μm) in LCE matrix and the 3D-printing system was developed by integrating a permanent magnet with 3-DoF motion into an extrusion-based 3D printer. The nematic order of the extruded filament can be programmed by controlling the print velocity, whereas the magnetization can be programmed by manipulating the magnet, leading to independent programming of both functional domains with anisotropy, referred to as dual anisotropy (Figure 1b). UV light was employed to quickly cure the extruded magLCE ink such that the programmed alignment was locked in situ. The magLCE can be actuated either by a magnetic field **B**, environmental heat, or photo-heating of the embedded NdFeB microparticles (Figure 1c), which enables multimodal shape-morphing under different actuation sequences of magnetic field and temperature change (Figure 1d). The magLCE shows a high energy density (2.25×10^5 J m^{-3}) and a tunable actuation temperature (24 and 94 °C). We designed a programmed magLCE strip robot with enhanced adaptability to complex environments (different terrains, magnetic fields, and temperatures) via a multiactuation strategy. Furthermore, the magLCE has potential applications in mechanical memory, as demonstrated by the multistable mechanical metastructure array with remote writability and stable memory.

2. Results and Discussion

The magLCE ink was fabricated by dispersing NdFeB microparticles into a photopolymerizable RM82–*n*-butylamine LCE matrix with an NdFeB volume fraction of 6% (Figures S1 and S2, Supporting Information). The reason for selecting such a low volume fraction was to retain the pristine cross-linking kinematics while imparting magnetic responsiveness to the LCE matrix. For example, both pure LCE and 6 vol% magLCE underwent rapid cross-linking within 10 s under UV light, as reflected by a steep change in viscosity (**Figure 2**a). If more NdFeB is doped (e.g., 12 vol%), the cross-linking of the LCE requires a longer time, which is not favorable for locking the programmed functional domains. Differential scanning calorimetry tests show that the magLCE ink has a glass-transition temperature (T_g) of −21 °C and a nematic–isotropic transition temperature (T_{NI}) of 85 °C, which are also extremely close to that of pure LCE (Figure 2b). To ensure suitable rheological properties for extrusion (e.g., relatively low viscosity with shear-thinning effect[18a,22]), a heater is integrated into the printhead to maintain the magLCE ink at a temperature of 55 °C (Figure S3, Supporting Information). Therefore, magLCE can be successfully printed (Movie S1, Supporting Information) with dispersed magnetized particles without aggregation (Figure S4, Supporting Information), unchanged LCE composition (as validated by the identical infrared spectroscopy in Figure S5, Supporting Information), and mechanical properties similar to pure LCE (Figure S6, Supporting Information).

A cylindrical magnet (diameter: 80 mm, length: 60 mm, and residual magnetization: 1.44 T) was employed as the source of the magnetic field to program the magnetization of the printed magLCE. The magnetizing field is denoted as $\mathbf{B}_m$. The magnet is mounted on a 3-axis stage that can effectively adjust the distance between the printer nozzle and magnet (denoted as d) as well as the orientation of the magnet including both in-plane rotation (denoted as angle α) and out-plane rotation (denoted as angle β) (Figure 2c; Figure S7, Supporting Information). In contrast to 3D printers, in which the nozzle moves on a fixed printing platform, we fixed the printhead and developed a 3-axis mobile printing platform. Thus, the nozzle is always aligned with the center of the magnet during printing, rendering the programming magnetic flux density B_p dependent only on distance d. As shown

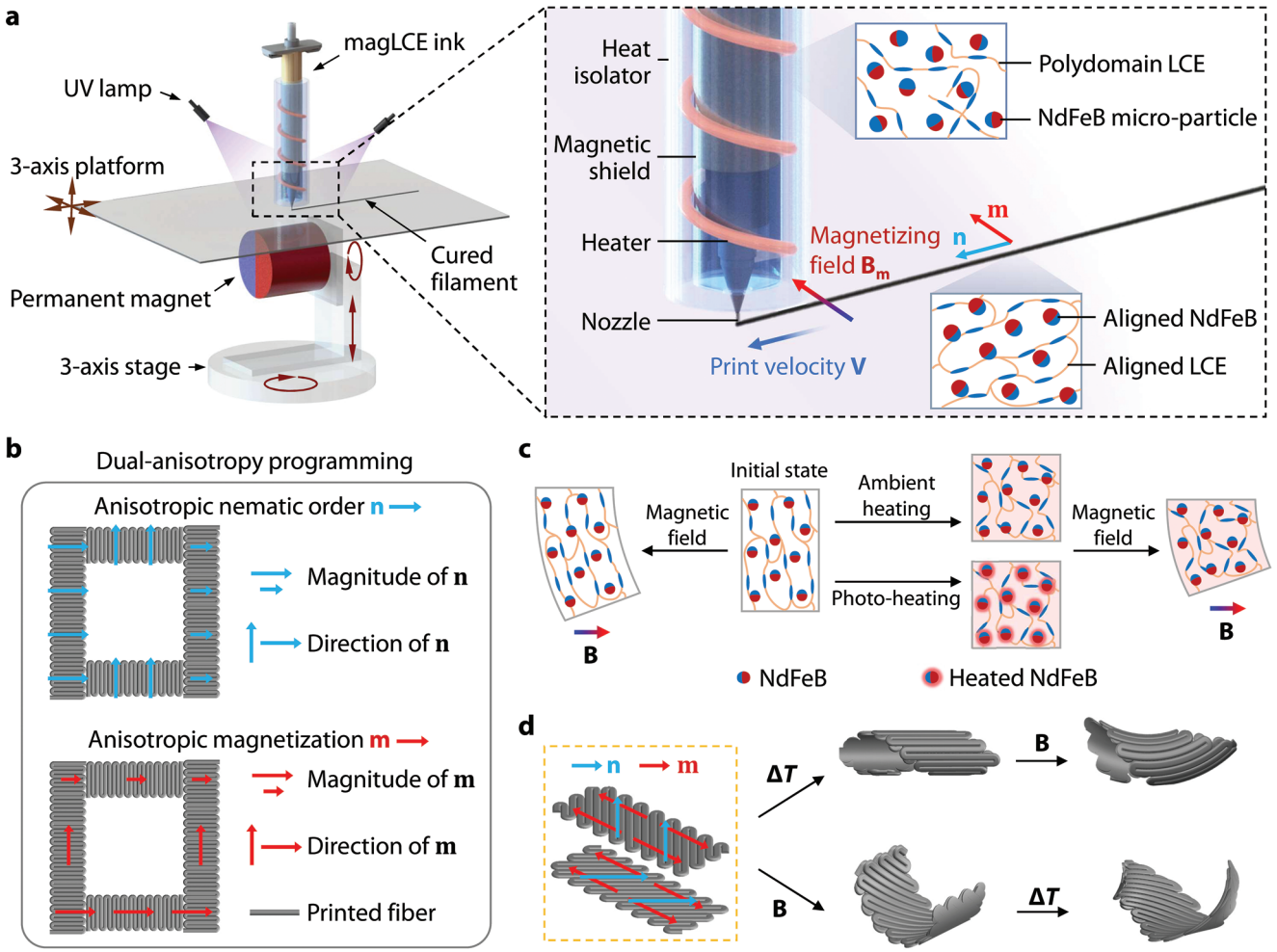

Figure 1. 3D printing of magLCE with programmed dual anisotropy and multimodal shape morphing. a) Schematic of customized 3D-printing system consisting of a fixed printhead, a 3-axis platform, a permanent magnet, and UV lamps. The magnetization **m** and nematic order n of magLCE are programmed by tuning the print velocity **V** and magnetizing field $\mathbf{B}_m$, respectively. The UV light quickly cross-links the printed filament, which locks the programmed alignment. b) Both nematic order and magnetization can be programmed to be anisotropic, i.e., with different directions and magnitudes. c) The magLCE can be actuated either by magnetic field **B**, environmental heat, or photo-heating of the embedded NdFeB microparticles. d) The dual anisotropy of the programmed magLCE enables multimodal shape-morphing under different sequences of an actuation magnetic field and temperature change.

in Figure 2d, the contour plots of $\mathbf{B}_m$ at $\alpha = 0°$, 45°, 90° are the same and changing α only alters the direction of $\mathbf{B}_m$ at the nozzle. By controlling the distance d, the magnetizing field strength B_m could be tuned up to 90 mT (Figure 2e). Before extrusion, the NdFeB microparticles inside the magLCE ink were randomly dispersed owing to the magnetic shield around the printhead; therefore, the magLCE ink had zero magnetization. After extrusion, the magnetizing field reorients the NdFeB particles, leading to a tunable magnetization strength of the magLCE filament up to $m = 31.5$ kA m^{-1} when $B_m = 90$ mT (Figure 2f).

The prepared magLCE was isotropic, with randomly distributed LCE mesogens. After extrusion from the nozzle (diameter 300 µm, print pressure 300 kPa), the mesogens were aligned along the print direction because of the shear force inside the nozzle,[23] transforming them to a nematic state. For a given nozzle under constant print pressure, the magnitude of the nematic order depends only on the print speed V. In general, a higher print speed yields a larger magnitude of nematic order, also known as the order parameter. This is because the aligned mesogens remain aligned and are further stretched after deposition at high print speeds. The nematic order can be observed using a polarized optical microscope. In summary, the polarized optical microscope shows brighter layers when polarized along the direction of the nematic order, whereas dark layers are observed in other directions. For example, at a high print speed $V = 5$ mm s^{-1}, the printed filament showed much brighter layers along the print direction than along the 45°/135°direction (Figure 2g). By contrast, when the printing speed was low, the extruded magLCE ink aggregates were misaligned with the mesogens and diminished the nematic order (Figure S8, Supporting Information). The nematic order determines the contraction capability of the magLCE when the temperature exceeds the nematic-to-isotropic transition temperature, T_{NI}. We can observe that the maximum contraction strain of the magLCE filament

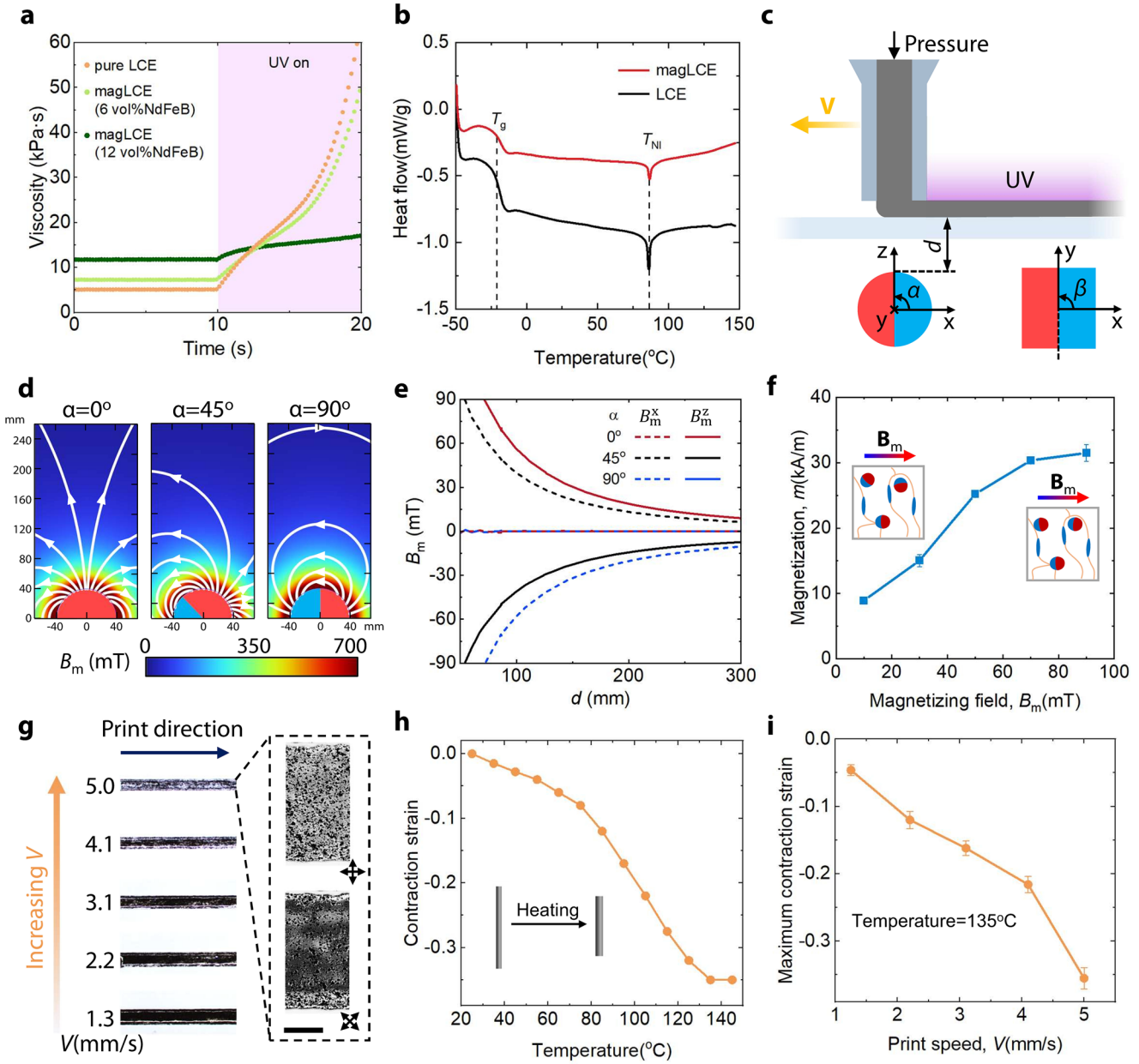

Figure 2. Programming of magnetization and nematic order. a) Viscosity changes under UV light for pure LCE and magLCE with 6 vol% and 12 vol% NdFeB. b) DSC tests of pure LCE and magLCE with 6 vol% NdFeB. The glass-transition temperature (T_g) is −22 °C, and the nematic–isotropic transition temperature (T_{NI}) is 87 °C. c) Schematic illustration of programming the magnetization by tuning the position and orientation of a cylindrical magnet. d) Simulated contour plot of magnetizing field $\mathbf{B}_m$ at $\alpha = 0°$, 45°, and 90°. e) Simulated magnetic flux density B_p as a function of distance d. The maximum B_p is 90 mT. f) Magnetization magnitude m as a function of programming magnetic flux density B_m. g) Increasing the printing velocity increases the nematic order of the printed filament along the print direction. The high nematic order in the print direction is reflected by the brighter layer according to polarized optical microscopy. The inset arrow denotes the polarization direction. Scale bar: 100 μm. h) Contraction strain of magLCE filaments printed at $V = 5$ mm s^{-1} under different ambient temperatures. i) Maximum contraction strain of magLCE filament as a function of print velocity at 135 °C.

printed at $V = 5$ mm s^{-1} is 35.5% when the ambient temperature reaches 135 °C on a hot plate (Figure 2h), which is 88.5% of the mechanically aligned counterpart (Figure S9, Supporting Information). In addition, the maximum contraction strain of 3D-printed magLCE was 92.0% of its pure LCE counterparts, suggesting that the 3D-printing technique can retain the large contraction strain of LCE bases. When the print speed was lower, the maximum contraction strain was correspondingly reduced owing to the small nematic order (Figure 2i).

The light absorption of pure LCE was ≈20% in the range of 500–1000 nm. By embedding NdFeB microparticles, the light absorption of magLCE reaches up to 92% (Figure S10,

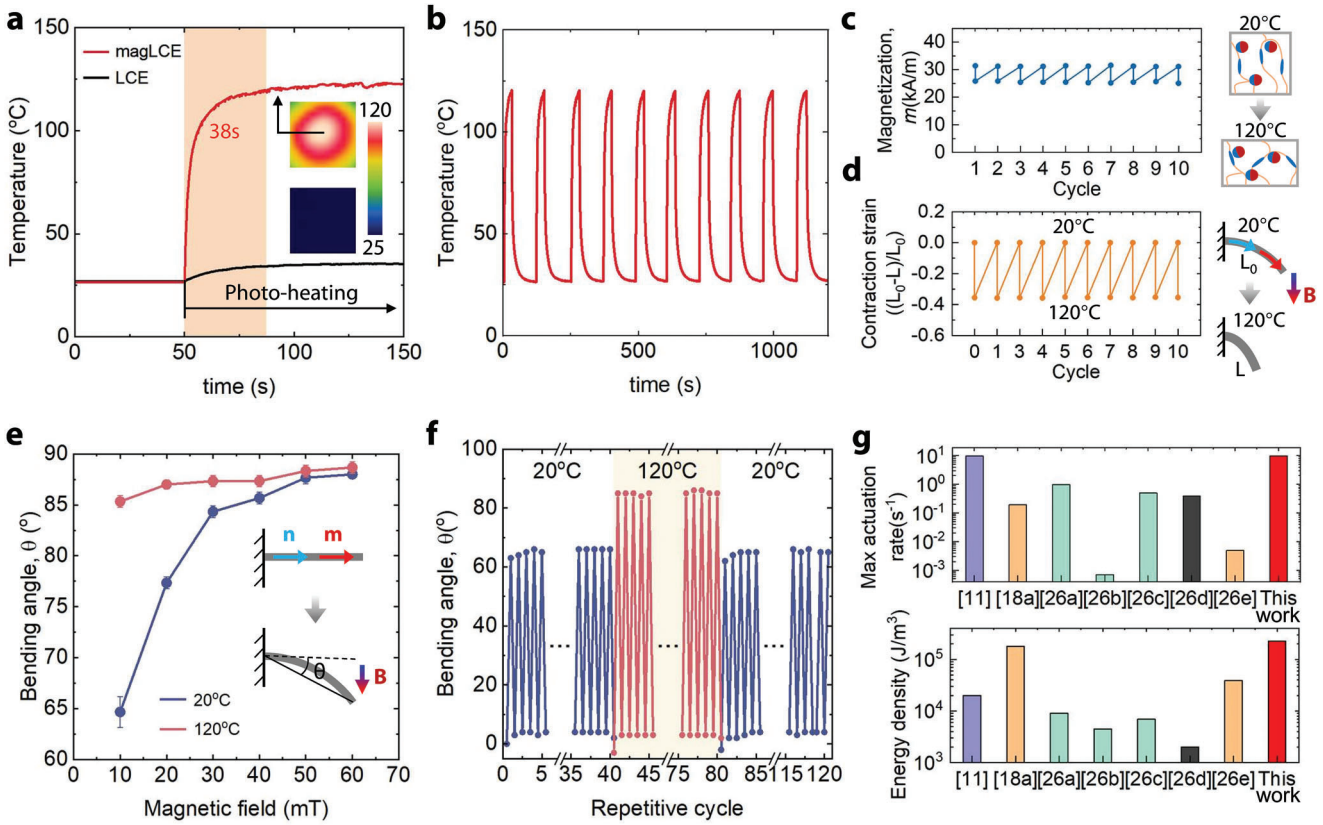

Figure 3. Characterization of magLCE. a) Photothermal effect of magLCE and pure LCE under an 808 nm near-infrared laser. b) Repetitive photoheating of magLCE. c) Magnetization strength *m* of the magLCE filament at 20 and 120 °C for 10 cycles. d) Contraction strain of magLCE filament at 20 and 120 °C for 10 cycles under magnetic field $B = 60$ mT. e) Bending angle of magLCE filament as a function of actuation magnetic fields at different temperatures. f) Repetitive actuation of magLCE for 120 cycles. g) Energy density and maximum actuation rate of magLCE compared with other 3D-printed active soft materials.

Supporting Information). Therefore, NdFeB microparticles can also function as photothermal agents under near-infrared light to trigger the nematic-to-anisotropic transition of magLCE.[24] As shown in **Figure 3**a, when exposed to an 808 nm laser with a light intensity of 10 mW mm^{-2}, the temperature of magLCE quickly increases and reaches a plateau of 120 °C within 38 s, which is considerably higher than that of a pure LCE (≈35 °C). This significant photothermal effect is also repeatable, as evidenced by the cyclic photoheating shown in Figure 3b. Notably, despite the large contraction strain, heating did not significantly affect the magnetization within 10 cycles (Figure 3c), which enabled the heated magLCE to be further actuated by magnetic fields. Furthermore, the magnetically induced macroscopic deformation did not significantly affect the nematic order at the microscopic scale, as validated by the unchanged maximum contraction strain (≈35%) of magLCE in a magnetic field $B = 60$ mT (Figure 3d). Consequently, the magnetization and nematic order of magLCE are roughly independent of each other at the microscopic level. On the other hand, the heated magLCE has a lower modulus owing to the phase transition from the nematic to the isotropic state.[25] Therefore, compared with that at 20 °C, the heated cantilever magLCE beam shows a larger bending angle under the same magnetic field (Figure 3e). Both the heating and magnetic actuation are reversible. We show that in a 120-cycle test, the bending angle remains the same before and after cyclic actuation at 120 °C (Figure 3f). Enabled by the large contraction strain and magnetic responsiveness, the magLCE also shows a high energy density of 2.25×10^5 J m^{-3} and a large actuation rate (0.1 s^{-1}), which are among the highest values compared with existing 3D-printed active materials (Figure 3g).[11,18a,26]

In general, dual actuation by magnetic fields and temperature has two synergetic effects on the macroscopic deformation of magLCE: 1) magLCE exhibits different modes of shape morphing under different stimulus sequences; 2) magLCE generally undergoes more pronounced deformation when subjected to two stimuli than a single stimulus. The synergistic effects can be described as follows. First, the magnetic field and temperature are intrinsically independent actuation mechanisms (Figure 3c,d); thus, the first applied stimulus produces an intermediate configuration (different from the initial configuration), which is further transformed into another when a subsequent stimulus is applied. Second, the heated magLCE had a much lower modulus, such that a larger deformation could be generated under the same magnetic field (Figure 3e). First, we present a single magLCE filament with opposite magnetization profiles in **Figure 4**a. At 20 °C, the magLCE filament can be bent by applying a magnetic field. Alternatively, if first heated to 120 °C, the magLCE filament contracts. Further

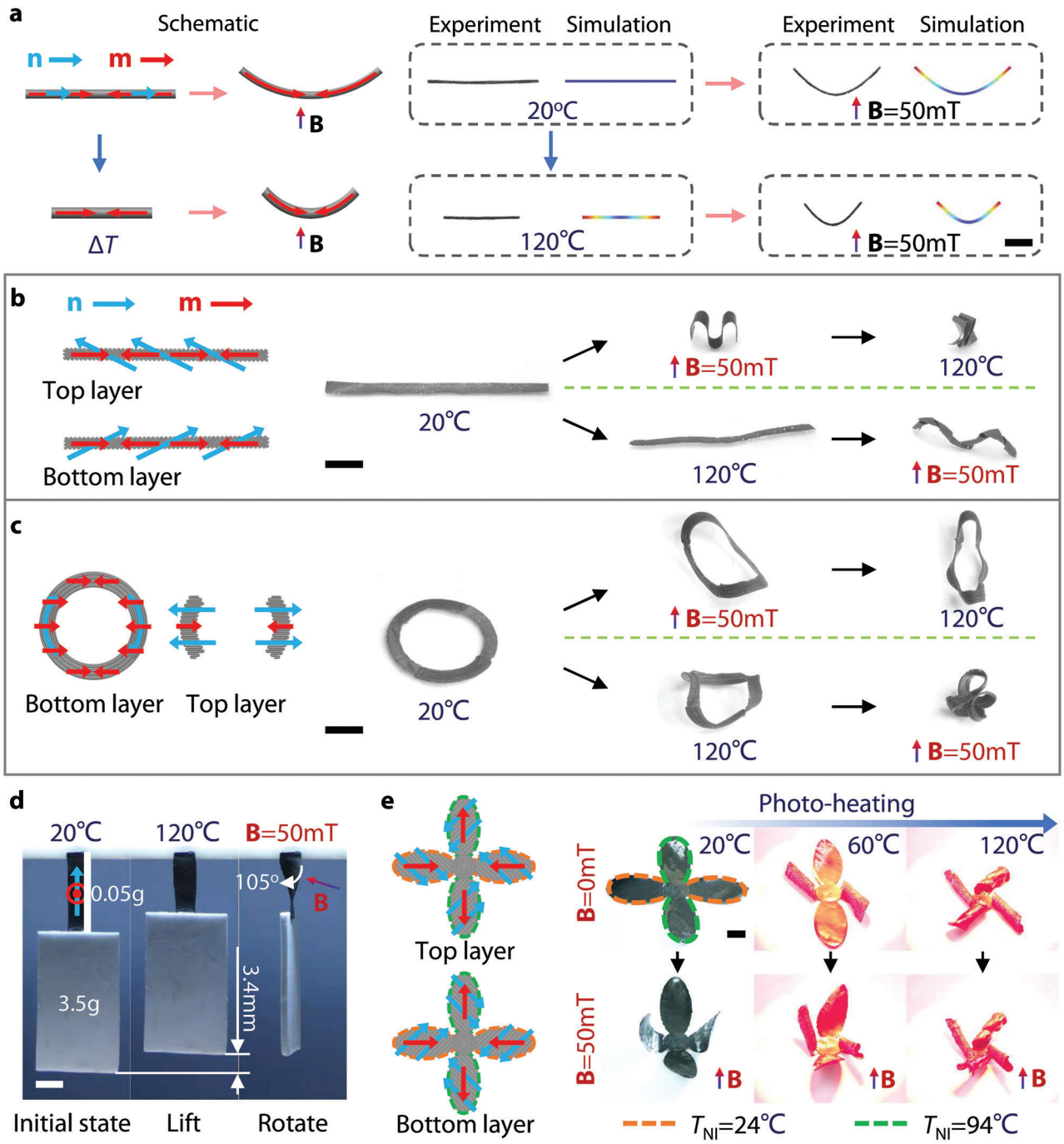

Figure 4. Multimodal shape morphing of magLCE with dual anisotropy. a) Experiments and finite element simulations of a magLCE filament with opposition **m**. Scale bar = 2 mm. b) Multimodal shape morphing of a bilayered rectangular beam under different actuation sequences. Scale bar = 10 mm. c) Multimodal shape morphing of a bilayered circle under different actuation sequences. Scale bar = 10 mm. d) Sequential images of a magLCE actuator (0.05 g) that lifts and rotates a 3.5 g object by increasing the temperature and applying a magnetic field. Scale bar = 5 mm. e) Sequential actuation of a four-petal magLCE flower with different T_{NI}. Scale bar = 5 mm.

magnetic actuation bent the filament to a larger curvature. Finite element simulations were conducted to elucidate the synergetic effect of dual-actuation for the magLCE filament, which was also validated experimentally (Figure 4a; Figure S11, Supporting Information). Notably, however, magnetic and temperature actuations do not interfere with each other at the microscopic scale, they may compete for macroscopic deformation, for example, heat-induced contraction compromises the deformation by magnetic fields. An example of a bilayered magLCE strip is presented in Figure 4b. At 20 °C, applying a magnetic field *B* first transforms the straight strip into an "M" shape. Further heating resulted in a highly curled M-shaped

strip. However, if first heated, the straight strip first curls along its body, increasing the structural rigidity of the strip such that the subsequent magnetic field only deforms the curled strip a bit, leading to an "M" shape with smaller deflection.

Another bilayer magLCE circle is shown in Figure 4c. Similarly, different actuation sequences of the magnetic field and heat generated different modes of shape morphing, and the synergistic effect was dominant. The high-energy-density, enables the magLCE to lift a 3.5 g object that is seven times its weight when heated to 120 °C (Figure 4d). Further application of a magnetic field can even rotate the lifted object, demonstrating its multimodal shape-morphing capability and synergetic effect. In addition, the nematic-to-isotropic temperature of the magLCE can be readily tuned by changing the active components of the LCE, which enables local actuation of the magLCE under different temperatures. For example, as shown in Figure 4e and Movie S2 (Supporting Information), we fabricate another type of magLCE with T_{NI} of 24 °C according to ref. [27] and assemble a bilayer magLCE flower with four petals. The two horizontal petals have a 24 °C T_{NI} (denoted by the yellow boundary) and the two vertical petals have 94 °C (denoted by the green boundary). By photo-heating using a near-infrared laser (808 nm), the horizontal petals will first curl at 60 °C owing to the lower T_{NI}, followed by the curling of vertical petals when the temperature reaches 120 °C. The curled magLCE flower can be further actuated by magnetic fields, which lead to the upward bending of the four petals, showing multimodal shape-morphing of the magLCE flower. Because the bending rigidity of the petals increases when they are heated to curl, their bending behavior is compromised by the subsequent magnetic field, suggesting a competing effect on the macroscopic deformation.

The magLCE, with its programmed dual-anisotropy and multi-responsiveness, can be used to fabricate soft robots with various shape morphing and environmental adaptability. In this study, we designed and demonstrated a magLCE strip robot that can adapt to complex environments (e.g., different terrains, magnetic fields, and temperatures). The strip robot has harmonic magnetization along the body and an orthogonal nematic order between the two layers (**Figure 5**a). The strip robot can be manipulated using magnetic fields at room temperature. Here, a cubic NdFeB magnet (N52, width: 3 cm, residual flux density Br = 1.44 T) is integrated into the robotic arm; therefore, the strip robot can be controlled with high stability and repeatability (Figures S12 and S13 and Movie S3, Supporting Information). As shown in Figure 5a, when the magnet is placed below the strip robot with its north-pole facing the robot ($B_x = 0$ mT, $B_y = 30$ mT), the robot arches up. By translating the magnet in the *x*-direction, the robot follows along with the movement of the magnet (Figure 5a). The displacements of the magnet and the center of the strip are denoted as *D* and *d*, respectively. By flipping the magnet while increasing B_y to −55 mT, the strip robot deforms into a "C" shape. Further rotation of the magnet causes both B_x and B_y to change sinusoidally, enabling the strip robot to roll at room temperature (Figure 5b). Placing the strip robot on a hot plate causes it to twist owing to the orthogonal contraction of magLCE. When the plate temperature T_{plate} reaches 100 °C, the robot transforms into a straight tubular shape. Applying a magnetic field to the magnet (similar to that in the rolling mode, $B_x = 0$ mT, $B_y = 55$ mT) causes the straight tubular robot to curve slightly. Further rotation of the magnet causes the curved tubular robot to twist forward with the rotating magnetic field (Figure 5c). In addition to magnetically actuated motion, the tubular robot can self-propel without magnetic fields when the hot plate temperature T_{plate} is increased to 150 °C. At such a high temperature, a large temperature gradient is generated between the top and bottom surfaces of the tubular robot, leading to a slight curvature along its body. The curved tubule tends to expand into a straight tubule, causing it to twist along its convex side on a hot plate (Figure 5d).[28] Owing to its various shape-morphing capabilities, a strip robot can adapt to different environments in sequential modes. As shown in Figure 5e and Movie S4 (Supporting Information), the strip robot is initially placed on a 20 °C flat surface. The robot can first crawl forward by manipulating a magnet. When it reaches an obstacle, it rolls across it under a rotating magnetic field. when it reaches the 100 °C hot plate, it morphs into a tubular shape. A rotational magnetic field is applied to twist the tubular robot forward. When it reaches a zone where the magnetic field is shielded, it can be further actuated via self-propelling by heating the plate to 150 °C. These motion sequences indicate that the magLCE robot can achieve multimodal locomotion by using different actuation sources to adapt to different complex environments. Independently programmable magnetization and LCEs nematic order enable magLCE soft robots with previously inaccessible multifunctionalities. Figure S14 and Movie S5 (Supporting Information) show a 3D-printed, bilayered, and cross-shaped magLCE robot that can transport cargo. First, the magLCE can walk under magnetic actuation. It can grab objects of different shapes upon heating. Subsequently, it can resume walking with the cargo under magnetic actuation. This cargo-transporting function cannot be realized using pure magnetic soft materials, pure LCE, or magLCEs fabricated using the conventional molding method. For example, robots fabricated using pure soft magnetic materials and pure LCE can only walk and grab objects. The molded MagLCE robot cannot grab the object because of the absence of an anisotropic nematic order.

Mechanical metastructures with stable and reprogrammable memory capabilities are attractive for robotic systems and data processing.[29] The dual-anisotropy and multi-responsiveness of the printed magLCE provide a promising integrated actuator for mechanical metastructures with remote control and memory capabilities. Herein, we present a multistable mechanical metastructure (MMM) that can be remotely reprogrammed between three states with stable memory. The MMM unit comprises four components: (i) a soft lid, (ii) a 3D-printed magLCE actuator, (iii) a clutch with stiff beams, and (iv) a pedestal (**Figure 6**a; Figure S15, Supporting Information). The upper side of the magLCE actuator is connected to a soft lid, whereas the lower side is connected to a clutch. The soft lid is fixed to the pedestal, and the clutch can be placed on the pedestal at three different gear positions: gears 1, 2, and 3, which correspond to states 1, 2, and 3, respectively, of the MMM unit. All the three states are stable. The MMM unit starts in state 1. To switch between different states, the magLCE actuator is first heated using a near-infrared laser to lift the clutch. The clutch is then rotated by applying a magnetic field. In addition, cooling the rotated magLCE actuator extends it, finalizing the gear switching (e.g., from 2 to 3, as shown in Figure 6b; Figure S16 and Movie S6, Supporting Information). The state of the MMM unit is locked by the

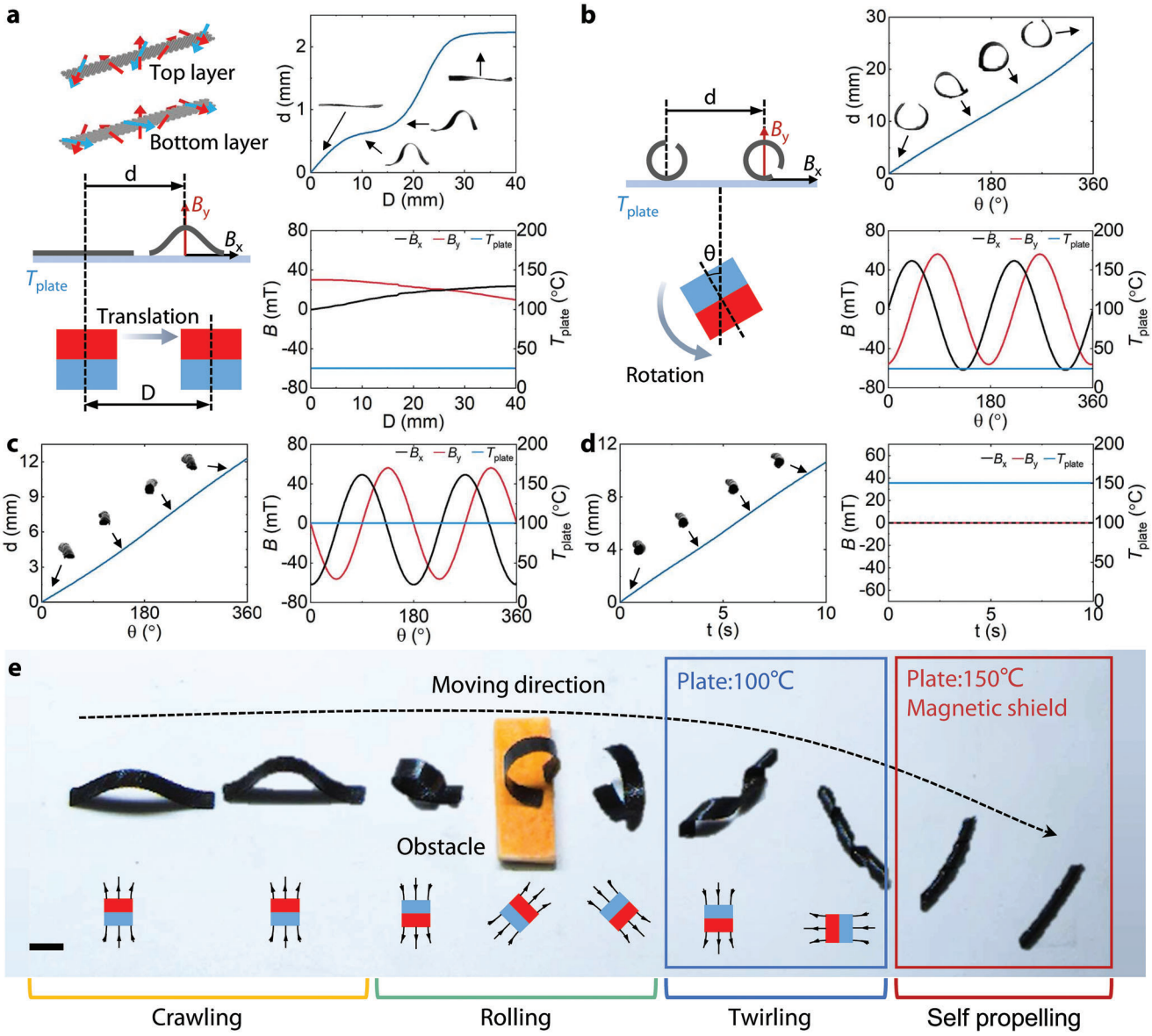

Figure 5. Demonstration of a 3D-printed magLCE strip robot with various shape-morphing capabilities and enhanced environmental adaptability. a) Crawling locomotion by translating the magnet toward the *x*-direction. b) Rolling by rotating the magnet at room temperature. c) Twirling on a 100 °C hot plate by rotating the magnet under. d) Self-propulsion on a 150 °C hot plate without magnetic fields. e) The robot sequentially crawls, rolls beyond an obstacle, twirls on the hot plate by applying magnetic field and is self-propelled by the environment-induced temperature gradient. Scale bar: 7 mm.

gear and cannot be changed by simply rotating or compressing it (Figure 6c). To switch the gear, the clutch must first be lifted by the NIR laser and subsequently rotated by a magnetic field, exhibiting nonvolatile memory. In different states, the mechanical behavior of an MMM unit under compressive loading is different. In state 1, the compressive plate only contacts the soft lid; in state 2, the compressive plate contacts the soft lid and stiff beam in sequence; and in state 3, the compressive plate contacts both the soft lid and stiff beam at the beginning (Figure 6d). The compressive forces (denoted as F_1, F_2, and F_3) as a function of the displacement for each state are shown in Figure 6e. By remotely applying magnetic fields and near-infrared lasers, the mechanical metastructure can switch states, yielding different mechanical force-displacement behaviors that can be used as mechanical memory. We fabricated a 3 × 3 MMM array and demonstrated five different combinations of states (Figure 6f). This combination can be expressed as (*i*,*j*,*k*), where *i*, *j*, and *k* represent the number of MMM units in states 1, 2, and 3, respectively. For example, the combination of (4,4,1) means that four MMM units are in state 1, four MMM units are in state 2, and one MMM unit is in state 3. The mechanical behaviors of the five combinations of the 3 × 3 MMM array are shown in Figure 6g. The total compressive force of the 3 × 3 MMM array can be estimated using $iF_1 + jF_2 + kF_3$. At compressive displacement of 0.3 mm (state ①

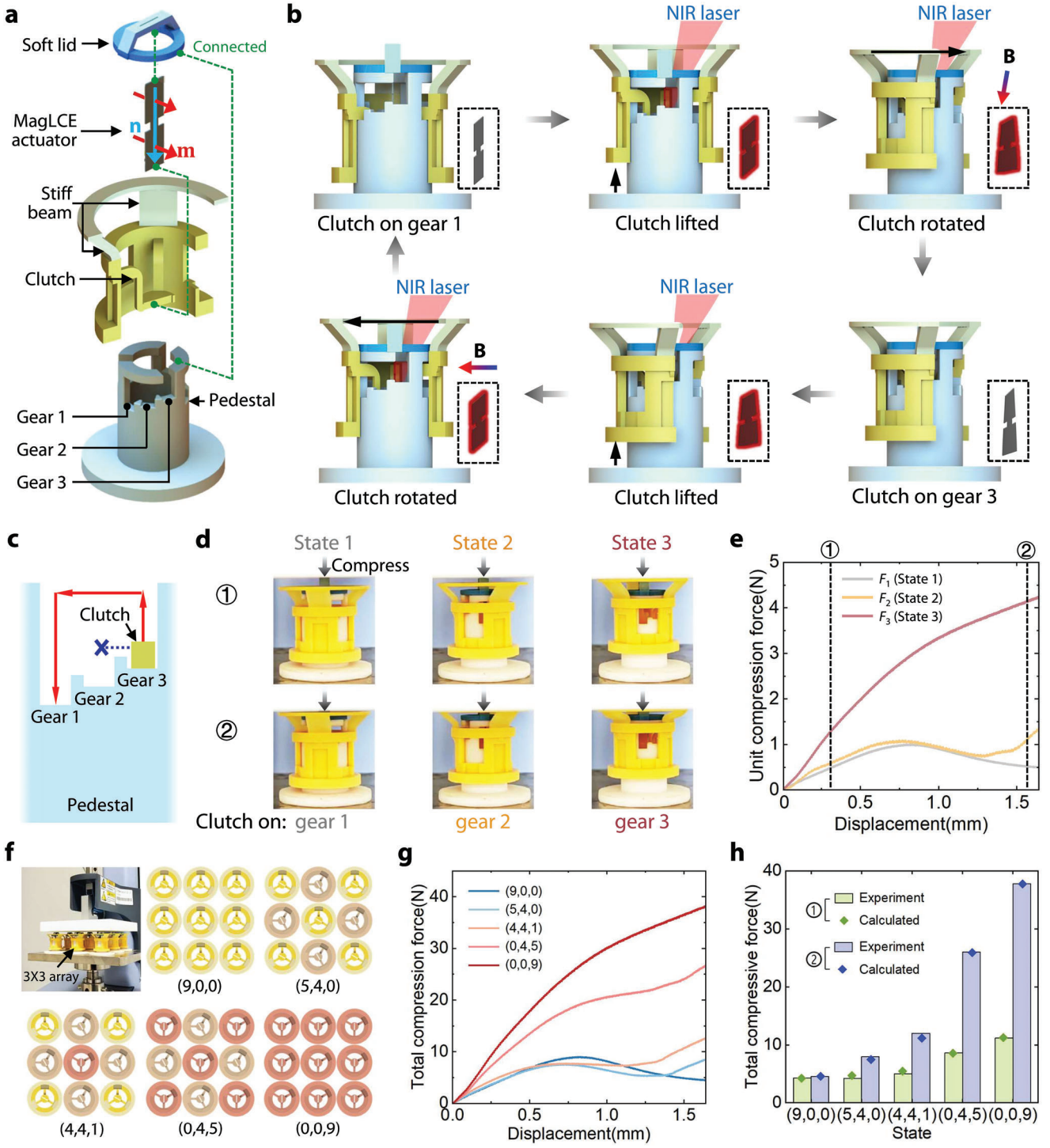

Figure 6. MagLCE-based mechanical metastructure with multistate memory. a) A multistable mechanical metastructure unit (MMM unit) consists of a soft lid fixed on a pedestal, a magLCE actuator, and a stiff beam sitting on the pedestal with three different gears. b) When heating the magLCE actuator with an NIR laser, the magLCE actuator contracts, causing the MMM unit to switch from one stable state to another stable state. c) Schematic illustration of the nonvolatility memory of the MMM unit. d) Images of the three stable states under the compression test. State ① corresponds to the displacement at 0.3 mm, and State ② corresponds to the displacement at 1.6 mm. e) The MMM unit at different states shows different force–displacement curves. f) Different combinations of a 3 × 3 MMM array. g) Force displacement of the 3 × 3 MMM array with five different combinations of unit states. h) Comparisons between experiments and calculations of forces at State ① (displacement 0.3 mm) and State ② (displacement 1.6 mm) for different combinations of the MMM array.

in Figure 6d) and 1.6 mm (state ②), the calculated results are in good agreement with the experimental results (Figure 6h). The magLCE enables simple rewritability of nonvolatile mechanical memory, and the information density can be further increased by increasing the number of gears.

3. Conclusion

We have developed a ferromagnetic LCE (magLCE) ink and designed a corresponding printing platform by integrating a magnet with 3-DoF motion into an extrusion-based 3D printer. By manipulating the magnetizing field and printing speed, the direction and strength of the nematic order and magnetization can be programmed individually. The printed magLCE exhibits multimodal shape-morphing under different sequences of stimuli (e.g., magnetic field, ambient heating, and photo-heating), a high energy density (2.25×10^5 J m^{-3}), and a tunable actuation temperature. In addition, we demonstrated the application of programmed magLCEs in soft robotics and mechanical memory. This work offers a new design and fabrication freedom for materials with magnetic and LCE advances.

4. Experimental Section

Ink Preparation: The LCE was synthesized by a previously reported aza-Michael addition method.[18a] As received, the diacrylate LC monomer, 1,4-bis-[4-(6-acryloyloxy-hexyloxy)benzoyloxy]-2-methylbenzene (RM82, Zhende Chemical Technology Inc.) and *n*-butylamine (Sigma–Aldrich) with a 1.1:1 mole ratio were added into a 50 mL round-bottom flask, followed by adding 2 wt% butylated hydroxy toluene (Sigma–Aldrich) and 2 wt% Irgacure 651 (BASF). The flask was filled with nitrogen and stirred at 105 °C for 18 h in the absence of light. The LCE with T_{NI} = 24 °C used in Figure 4e was synthesized by a previously reported thiol-acrylate "click" reaction.[27] As received, 2,2′-(ethylenedioxy)diethanethiol (EDDT, Sigma–Aldrich), RM82, 1,4-bis-[4-(3-acryloyloxypropypropyloxy) benzoyloxy]-2-methylbenzene (RM257, Zhende Chemical Technology Inc.), and 1,3,5-triallyl-1,3,5-triazine-2,4,6(1H,3H,5H)-trione (TATATO, Sigma–Aldrich) was added into a 25 mL round-bottom flask in a mole ratio of 1.0:0.6:0.2:0.133, followed by adding 1 wt% triethylamine (TCI), 2 wt% butylated hydroxytoluene (Sigma–Aldrich), and 1.5 wt% Irgacure 651 (BASF). All materials were melted with a heat gun and blended for 5 min. Then, the flask was filled with nitrogen and stirred at 65 °C for 3 h in the absence of light. The LCE with T_{NI} = 24 °C was stored at −18 °C before printing.

NdFeB microparticles with an average size of 5 µm (MQFP-B+, Magnequench) were added into the as-synthesized LCE ink followed by manual stirring. Then, the mixture was heated to 90 °C and blended with a planetary mixer (ARV-310, Thinky) at 2000 rpm. for 2 min. The well-mixed magLCE ink was transferred into 10 ml syringe barrels and degassed in a vacuum oven overnight. Before printing, the ink was magnetized by an impulse magnetizer (M20-2020, HLT Co. LTD) with ≈2.8 T magnetic field.

Characterization of Inks: Rheological characterization of magLCE and LCE inks was performed on a rotational rheometer (Physical MCR 301, Anton Paar, Austrian), and a 20 mm steel Peltier plate was used with a 0.5 mm gap distance. For each test, samples were heated to 120 °C to erase the temperature history and kept at the measurement temperature (i.e., 25 or 55 °C) for 5 min before measurement. During the viscosity measurement, the shear rate was swept from 10^{-2} s^{-1} to 10^{2} s^{-1}. During the oscillatory measurement, the shear stress was swept from 1 to 10^{4} Pa at 1 Hz. The viscosity change under UV explosion was conducted with a 0.07 mm gap distance. A glass base of the rheometer was used to transparent UV light (generated by Omnicure S2000, Excelitas) with a light intensity of 20 mW mm^{-2}. A constant shear rate of 1 s^{-1} was used during the measurement. For differential scanning calorimetry, the LCE ink was heated to 120 °C to erase any thermal history, cooled to −50 °C, and then heated to 200 °C, all at a rate of 10 °C min^{-1} (Q200, TA Instruments).

3D Printing of MagLCE: The 3D printing of magLCE was performed on a home-built 3D printer. The syringe barrel containing magLCE ink was mounted onto a fixed holder with a heater, a heat isolator and a magnetic shield. The building platform was mounted onto a 3-axis robotic arm. A cylinder NdFeB permanent magnet was mounted on a 3-axis motorized stage and placed below the platform, which could induce a magnetic field from 0 to 150 mT around the nozzle. The G-code was generated according to the designed model and modified with a MATLAB script to control the extrusion and movement of both the building platform and the permanent magnet. Stainless-steel nozzles with a 300 µm inner diameter were used for all printing experiments. During printing, the ink was heated and kept at 55 °C, and the air pressure used was 200 kPa. An on-the-fly UV light (Omnicure S2000, Excelitas) of ≈20 mW cm^{-2} was equipped. For magLCE ink with T_{NI} = 24 °C, it was kept at room temperature during printing, and the air pressure used was 450 kPa. After printing, the magLCE was postcross-linked under UV exposure (≈20 mW cm^{-2}) for 15 min on each side. To fabricate the mechanically aligned counterpart, magLCE ink was poured on a silicone (Dragonskin 10, Smooth on) mold and then heated to 120 °C to erase the temperature history. After being cooled to room temperature, the silicone mold was uniaxially stretched for 100% and cured with a 20 mW cm^{-2} UV light (Omnicure S2000, Excelitas).

Characterization of the Programmed MagLCE Actuator: SEM and EDS mapping images of the magLCE were taken with a scanning electron microscope (Hitachi, SU8220). The alignment of mesogens was characterized by a polarized optical microscope (DM4500P, LEICA). To measure the contraction strain of magLCE, the magLCE was placed on a hot plate covered with silica oil. The original length of the sample is first measured (denoted as L_0) and compared with the contracted length (denoted as L) measured at different temperatures (measured by the infrared camera) to calculate the heat-induced contraction strain. The alignment of NdFeB under different magnetic fields was characterized by measuring the magnetic moment density of the printed magLCE sample using a SQUID magnetic property measurement system (MPMS3, Quantum Design). Before testing, the printed samples were cut into 3 mm × 3 mm squares. The sample was kept at the measurement temperature for 5 min for stabilization before reading. The *B*–*H* loop of the printed magLCE was measured by sweeping the magnetic field from −3 to 3 T. The photothermal effect of the LCE and magLCE was characterized by heating them using an 808 nm laser (LR-MFJ-808/500 mW, Changchun Laser Technology) with an intensity of 20 mW mm^{-2}. An infrared camera (ETS320, FLIR) was used to record the temperature distribution during the heating process. The light absorption capability of magLCE and pure LCE was measured by a UV–vis–NIR spectrophotometer (SolidSpec-3700i/3700i, SHIMADZU).

Simulation of Programmed MagLCE Actuator: The FE simulation is performed in COMSOL multiphysics. The magLCE is considered a linear elastic material with anisotropic thermal expansion and magnetization. The thermal expansion coefficient α parallel to the nematic order is set as 35.5% according to Figure 2i, and the coefficient perpendicular to the nematic order is set as 0.5α. For magnetic actuation, the magnetization is set according to Figure 3c. The Poisson's ratio is set as 0.499. Young's modulus at room temperature is set as 3.67 MPs, as measured in Figure S6 (Supporting Information), and Young's modulus at 120 °C was set as half of that at room temperature, as previously reported.[25]

Actuation of MagLCE: The actuation of the printed magLCE actuator was conducted on an aluminum hotplate. For deformation characterizations and demonstrations, the actuators were placed in a glass Petri dish with silica oil (PMX-200, Dow Corning). The temperature of the hot plate was set to 180 °C so that the silica oil was stable at 120 °C, and the magnetic field was generated by a pair of home-built Helmholtz coils. For the actuation test in Figure 3c–f, a 10 mm × 3 mm × 0.14 mm filament was printed with nematic order and magnetization along its axial direction. For the repetitive test shown in Figure 3f, an actuation magnetic field perpendicular to the magnetization with strength B = 60 mT is used for all actuation cycles. For photothermal actuation of the magLCE flower, 808 nm infrared light with an intensity of 10 mW mm^{-2} was generated by an IR

light-emitting diode (IR808E, Hasun). For the actuation of the magLCE robot, the aluminum hotplate was covered by a glass plate, which was kept at room temperature when no thermal actuation was needed and heated to 120 °C for LCE deformation. The magnetic field was generated by a 30 mm × 30 mm × 30 mm cubic permanent magnet. A robotic arm (UR5e, Universal Robots) was used to move and rotate the permanent magnet. A CMOS camera (acA2440-20 gm/gc, Basler, Germany) was used to record the actuation process of the magLCE sample. The maximum actuation rate was obtained using the sample in Figure 4a, and the time between the application of the magnetic field and the time it reaches its largest deformation is recorded.

Calculation of Energy Density: The energy density induced by heating-induced contraction was calculated to evaluate the overall actuation performance of the printed magLCE. The energy density ρ_E is approximated by $\rho_E = E\varepsilon_a^2/2$, where $E = 3.67$ MPs is Young's modulus at room temperature and ε_a is the maximum contraction strain.[11,26e] As shown in Figure 2h, the maximum contraction strain is $\varepsilon_a = 35.5\%$, yielding an energy density of $\rho_E = 2.25 \times 10^5$ J m^{-3}. The energy densities of the 3D-printed LCE, hydrogel, HME, and GoE are directly obtained from refs. [11,18a,26].

Fabrication and Demonstration of the MMM Unit: The soft lid, clutch, and pedestal were fabricated using a Stratasys J7500 3D printer. Deformable parts of the soft lid and the clutch (stiff beams) were 40 A and 50 A shore hardness, respectively. The 3D-printed magLCE actuator was glued with the soft lid and the stiffener and then assembled with the pedestal. (Re)program and compression tests were performed for a single MMM unit and a 3 × 3 array. During the (re)writing process, an 808 nm infrared light with an intensity of 10 mW mm^{-2} was used to heat the magLCE actuator.

Supporting Information

Supporting Information is available from the Wiley Online Library or from the author.

Acknowledgements

This work was supported by the National Natural Science Foundation of China (Grant no. 51475442, no. 12272369), the National Key Research and Development Program of China (Grant no. 2020YFA0710100,2022FYC2408100), the Natural Science Foundation of Anhui Province (Grant no. 2108085ME170), and the Joint Funds from Hefei National Synchrotron Radiation Laboratory (Grant no. KY2090000068) and partially carried out at the USTC Center for Micro and Nanoscale Research and Fabrication, and Engineering Practice Center, University of Science and Technology of China. J.L. acknowledges the support from the Natural Science Foundation of Guangdong Province (2022A1515010152), the Basic Research Program of Shenzhen (JCYJ20210324105211032 and GJHZ20210705141809030), the Scientific Research Platforms and Projects of the University of Guangdong Provincial Education Office (2022ZDZX3019), and the Science, Technology, and Innovation Commission of Shenzhen Municipality (ZDSYS20200811143601004 and ZDSYS20220527171403009).

Conflict of Interest

The authors declare no conflict of interest.

Data Availability Statement

The data that support the findings of this study are available from the corresponding author upon reasonable request.

Keywords

3D printing, anisotropy, ferromagnetic materials, liquid crystal elastomers, programming

Received: March 27, 2023
Revised: July 6, 2023
Published online: September 21, 2023

[1] a) Y. Zhao, Y. Chi, Y. Hong, Y. Li, S. Yang, J. Yin, *Proc. Natl. Acad. Sci. USA* **2022**, *119*, e2200265119; b) G. Gu, J. Zou, R. Zhao, X. Zhao, X. Zhu, *Sci. Rob.* **2018**, *3*, eaat2874; c) X. Yang, W. Shang, H. Lu, Y. Liu, L. Yang, R. Tan, X. Wu, Y. Shen, *Sci. Rob.* **2020**, *5*, eabc8191; d) S. Zhang, X. Ke, Q. Jiang, H. Ding, Z. Wu, *Sci. Rob.* **2021**, *6*, eabd6107.
[2] a) E. J. Markvicka, M. D. Bartlett, X. Huang, C. Majidi, *Nat. Mater.* **2018**, *17*, 618; b) Y. Bai, H. Wang, Y. Xue, Y. Pan, J. T. Kim, X. Ni, T. L. Liu, Y. Yang, M. Han, Y. Huang, J. A. Rogers, X. Ni, *Nature* **2022**, *609*, 701; c) Y. Guo, J. Zhang, W. Hu, M. T. A. Khan, M. Sitti, *Nat. Commun.* **2021**, *12*, 5936.
[3] a) Y. Tang, M. Li, T. Wang, X. Dong, W. Hu, M. Sitti, *Adv. Mater.* **2022**, *34*, 2204185; b) L. Wang, C. F. Guo, X. Zhao, *Extreme Mech. Lett.* **2022**, *51*, 101604.
[4] a) K. M. Herbert, H. E. Fowler, J. M. McCracken, K. R. Schlafmann, J. A. Koch, T. J. White, *Nat. Rev. Mater.* **2021**, *7*, 23; b) M. Liu, L. Jin, S. Yang, Y. Wang, C. B. Murray, S. Yang, *Adv. Mater.* **2023**, *35*, 2208613.
[5] H. Kim, J. A. Lee, C. P. Ambulo, H. B. Lee, S. H. Kim, V. V. Naik, C. S. Haines, A. E. Aliev, R. Ovalle-Robles, R. H. Baughman, T. H. Ware, *Adv. Funct. Mater.* **2019**, *29*, 1905063.
[6] a) Y. Wang, R. Yin, L. Jin, M. Liu, Y. Gao, J. Raney, S. Yang, *Adv. Funct. Mater.* **2022**, *33*, 2210614; b) Y. Wang, A. Dang, Z. Zhang, R. Yin, Y. Gao, L. Feng, S. Yang, *Adv. Mater.* **2020**, *32*, 2004270.
[7] a) M. J. Ford, C. P. Ambulo, T. A. Kent, E. J. Markvicka, C. Pan, J. Malen, T. H. Ware, C. Majidi, *Proc. Natl. Acad. Sci. USA* **2019**, *116*, 21438; b) C. P. Ambulo, M. J. Ford, K. Searles, C. Majidi, T. H. Ware, *ACS Appl. Mater. Interfaces* **2021**, *13*, 12805.
[8] X. Pang, J. A. Lv, C. Zhu, L. Qin, Y. Yu, *Adv. Mater.* **2019**, *31*, 1904224.
[9] Q. He, Z. Wang, Y. Wang, A. Minori, M. T. Tolley, S. Cai, *Sci. Adv.* **2019**, *5*, eaax5746.
[10] a) Y. Kim, X. Zhao, *Chem. Rev.* **2022**, *122*, 5317; b) L. Wang, Y. Kim, C. F. Guo, X. Zhao, *J Mech Phys Solids* **2020**, *142*, 104045.
[11] Y. Kim, H. Yuk, R. Zhao, S. A. Chester, X. Zhao, *Nature* **2018**, *558*, 274.
[12] a) C. Zhou, Y. Yang, J. Wang, Q. Wu, Z. Gu, Y. Zhou, X. Liu, Y. Yang, H. Tang, Q. Ling, L. Wang, J. Zang, *Nat. Commun.* **2021**, *12*, 5072; b) T. Wang, H. Ugurlu, Y. Yan, M. Li, M. Li, A. M. Wild, E. Yildiz, M. Schneider, D. Sheehan, W. Hu, M. Sitti, *Nat. Commun.* **2022**, *13*, 4465; c) J. Zhang, Z. Ren, W. Hu, R. H. Soon, I. C. Yasa, Z. Liu, M. Sitti, *Sci. Rob.* **2021**, *6*, eabf0112; d) T. Xu, J. Zhang, M. Salehizadeh, O. Onaizah, E. Diller, *Sci. Rob.* **2019**, *4*, eaav4494.
[13] Y. Yang, J. Wang, L. Wang, Q. Wu, L. Ling, Y. Yang, S. Ning, Y. Xie, Q. Cao, L. Li, *Sci. Adv.* **2022**, *8*, eabq1456.
[14] W. Hu, G. Z. Lum, M. Mastrangeli, M. Sitti, *Nature* **2018**, *554*, 81.
[15] J. Zhang, Y. Guo, W. Hu, R. H. Soon, Z. S. Davidson, M. Sitti, *Adv. Mater.* **2021**, *33*, 2006191.
[16] Y. Li, H. Yu, K. Yu, X. Guo, X. Wang, *Adv. Funct. Mater.* **2021**, *31*, 2100338.
[17] a) Y. Sun, L. Wang, Y. Ni, H. Zhang, X. Cui, J. Li, Y. Zhu, J. Liu, S. Zhang, Y. Chen, M. Li, *Nat. Commun.* **2023**, *14*, 245; b) X. Peng, S. Wu, X. Sun, L. Yue, S. M. Montgomery, F. Demoly, K. Zhou, R. R. Zhao, H. J. Qi, *Adv. Mater.* **2022**, *34*, 2204890; c) X. Kuang, J. Wu, K. Chen, Z. Zhao, Z. Ding, F. Hu, D. Fang, H. J. Qi, *Sci. Adv.* **2019**, *5*, eaav5790.
[18] a) A. Kotikian, R. L. Truby, J. W. Boley, T. J. White, J. A. Lewis, *Adv. Mater.* **2018**, *30*, 1870063; b) A. Kotikian, C. McMahan, E. C.

Davidson, J. M. Muhammad, R. D. Weeks, C. Daraio, J. A. Lewis, *Sci. Rob.* **2019**, *4*, eaax7044.
[19] Z. Wang, Z. Wang, Y. Zheng, Q. He, Y. Wang, S. Cai, *Sci. Adv.* **2020**, *6*, eabc0034.
[20] Y. Dong, L. Wang, N. Xia, Z. Yang, C. Zhang, C. Pan, D. Jin, J. Zhang, C. Majidi, L. Zhang, *Sci. Adv.* **2022**, *8*, eabn8932.
[21] J. Chen, X. Liu, Y. Tian, W. Zhu, C. Yan, Y. Shi, L. B. Kong, H. J. Qi, K. Zhou, *Adv. Mater.* **2022**, *34*, 2102877.
[22] L. Li, Q. Lin, M. Tang, A. J. E. Duncan, C. Ke, *Chemistry* **2019**, *25*, 10768.
[23] M. Chen, M. Gao, L. Bai, H. Zheng, H. J. Qi, K. Zhou, *Adv. Mater.* **2022**, *35*, 2209566.
[24] H. Deng, K. Sattari, Y. Xie, P. Liao, Z. Yan, J. Lin, *Nat. Commun.* **2020**, *11*, 6325.
[25] Z. Wang, N. Boechler, S. Cai, *Addit. Manuf.* **2022**, *52*, 102678.
[26] a) J. Kim, J. A. Hanna, M. Byun, C. D. Santangelo, R. C. Hayward, *Science* **2012**, *335*, 1201; b) S. E. Bakarich, R. Gorkin, M. in het Panhuis, G. M. Spinks, *Macromol. Rapid Commun.* **2015**, *36*, 1211; c) L. Huang, R. Jiang, J. Wu, J. Song, H. Bai, B. Li, Q. Zhao, T. Xie, *Adv. Mater.* **2017**, *29*, 1605390; d) W. Li, F. Li, H. Li, M. Su, M. Gao, Y. Li, D. Su, X. Zhang, Y. Song, *ACS Appl. Mater. Interfaces* **2016**, *8*, 12369; e) S. Li, H. Bai, Z. Liu, X. Zhang, C. Huang, L. W. Wiesner, M. Silberstein, R. F. Shepherd, *Sci. Adv.* **2021**, *7*, eabg3677.
[27] M. O. Saed, C. P. Ambulo, H. Kim, R. De, V. Raval, K. Searles, D. A. Siddiqui, J. M. O. Cue, M. C. Stefan, M. R. Shankar, T. H. Ware, *Adv. Funct. Mater.* **2018**, *29*, 1806412.
[28] F. Zhai, Y. Feng, Z. Li, Y. Xie, J. Ge, H. Wang, W. Qiu, W. Feng, *Matter* **2021**, *4*, 3313.
[29] a) T. Chen, M. Pauly, P. M. Reis, *Nature* **2021**, *589*, 386; b) K. Bertoldi, V. Vitelli, J. Christensen, M. van Hecke, *Nat. Rev. Mater.* **2017**, *2*, 17066.